3D electromagnetic modeling explains apparent velocity increase in crosshole GPR data - borehole fluid effect correction method enables to incorporating high-angle traveltime data

Amirpasha Mozaffari, *Fellow, IEEE*, Anja Klotzsche, Zhen Zhou, Harry Vereecken and Jan van der Kruk., *Member, IEEE*

***Abstract* — For high-resolution crosshole ground-penetrating radar (GPR) tomography, a wide-range of ray path angles are required, including transmitter-receiver pairs with high-angles. However, artefacts have been observed in the inverted GPR tomograms when high-angle data were incorporated in ray-based inversion (RBI) tomography, due to not well-understood increasing apparent velocities for increasing ray-angles. To reduce these artefacts, it is common practice to limit the angular aperture to a threshold between 30° to 50°, which reduces the spatial resolution. We apply 3D finite-difference time-domain GPR modelling including borehole fluid and resistive loaded finite-length antenna models to study the increase of apparent velocity with increasing ray path angle. This study shows that the strong refraction of the electromagnetic waves at the borehole interface between water and subsurface is one of the reasons for these not well-understood phenomena. We introduce a novel borehole-fluid effect correction (BFEC) that relocates the transmitter and receiver positions to the location where the refraction is occurring to remove any influence of the borehole such that the remaining traveltimes can be inverted using an RBI. BFEC improves the estimated apparent-velocity (relative permittivity) values and enables the incorporation of wide-angle ray paths resulting in more accurate tomograms. We verify the BFEC for a homogenous and realistic synthetic model. By applying curved-ray RBI without and with the BFEC, the subsurface structures are reconstructed with more details for the BFEC data and average relative error model reduced from 13% to under 9% for the high-resolution inhomogeneous model.**

***Index Terms*— Antenna radiation patterns, Finite difference methods, Geophysics, Ground penetrating radar, Numerical simulation.**

I. Introduction

CROSSHOLE ground penetrating radar (GPR) has gained popularity as a tool for high-resolution imaging of the shallow surface (e.g., [1]–[4]). Whereas zero-offset measurements provide low-resolution images by using only horizontally traveling waves, high-resolution tomograms can be obtained from inverting data acquired by using a wide-range of ray path angles including transmitter-receiver's pairs that produce high-angle ray paths [5]–[7]. Limiting the angular aperture for subsurface imaging, results in a reduced spatial resolution of the tomogram[8]–[12].

However, artefacts have been observed in the inverted GPR tomograms when high-angle data were incorporated in ray-based tomography and inversions [13]. In addition to the increasing noise level that makes the picking of the first-arrival high-angle traveltimes more challenging, an increasing apparent velocity for increasing ray path angles has been observed, where the apparent-velocity was calculated by dividing the direct distance between transmitter and receiver over the first-arrival traveltime. [14] clearly showed a systematically increase in the recorded apparent velocity for increasing ray path angles, which was described as an "incompatibility of high-angle data". [13] reduced the artifacts in the inversion results by using only data with angular apertures up to 50° and ignoring high-angle data. [15] limited the ray path angles to 45° because of similar observations that they explained as a possible short circuit between the transmitter and receiver's communication cables installed in the boreholes. Another possible explanation was given by [16], who stated that the increasing apparent velocity for increasing ray path angle is caused by a higher wave velocity in the antennas compared to the wave velocity in the surrounding medium. In this way, waves emitted from the tip of the transmitter antenna traveling to the receiver antenna's tip have a faster ray path compared to waves directly traveling from the feed point of the transmitter antenna to the voltage gap of the receiver antenna.

[16] indicated that the high-angle waveform picks are distorted due to the finite-length antenna (FLA), the borehole-fluid effect, and difficulties to pick a correct first arrival due to a low signal to noise ratio. They also introduced a heuristic approach to incorporate the high-angle ray paths by using a traveltime correction curve as function of the ray path angle to compensate the increasing apparent-velocity for increasing ray path angle assuming the zero-angle ray path velocities being correct. We should note that this phenomenon has been only observed for GPR crosshole data, a seismic crosshole study carried out by [17] at the same test site did not show an increasing apparent-velocity with increasing ray path angle.

Since the study of [13], limiting the angular aperture to a particular threshold up to 30° to 50° became a standard pre-

Amirpasha Mozaffari, Anja Klotzsche Harry Vereecken and Jan van der Kruk are with Agrosphere (IBG-3), Institute of Bio- and Geosciences, Forschungszentrum Jülich GmbH, Germany and centre for High-Performance Scientific Computing in Terrestrial Systems, HPSC TerrSys, Geoverbund ABC/J, Jülich, Germany (e-mail: a.mozaffari@fz-juelich.de; a.kloztsche@fz-juelich.de; h.vereecken@fz-juelich.de; j.van.der.kruk@fz-juelich.de).

Zhen Zhou is a former member of Agrosphere (IBG-3), Institute of Bio- and Geosciences, Forschungszentrum Jülich GmbH, Germany. He is now with School of Information Engineering, ZheJiang A&F University, Hangzhou 311300, China. (e-mail: zhen.zhou12@outlook.com)

processing step for ray-based crosshole tomography inversion. Over 30 papers and studies use a limited angular aperture based on the findings of [13], [15], e.g., for ray-based tomography (e.g., [18], [19]), stochastic tomography (e.g., [20], [21]), time-lapse monitoring (e.g., [22], [23]) and full-waveform inversion (e.g., [24], [25]).

In summary, by including high-angle ray paths having increased apparent-velocities results in tomography inversion artifacts. However, by removing high-angle ray paths one significantly reduces the spatial resolution, so both options have a disadvantage. Several possible explanations for this increasing apparent velocity have been suggested, but no detailed study has been performed to investigate the actual cause of this phenomenon, probably due to the lack of available modeling codes and computer resources that enable including all the possible reasons in the analysis. Here, we investigate in detail the hypothesis that difficulties and inconsistency of high angle issue caused to some extent by refraction occurs in boreholes interface; by using a detailed 3D finite-different time-domain (FDTD) model that is able to include the presence of the borehole, borehole fluid and transmitter and receiver being resistive loaded finite-length antennas (RLFLA). In the following, we explain the physics and show a possible reason for the increase in apparent velocity for increasing ray path angle. Furthermore, we introduce a novel borehole-fluid effect correction (BFEC) method that returns improved apparent-velocity values such that also high-angle ray paths can be included in a ray-based tomography to obtain an improved traveltime inversion result.

II. Novel Pre-Processing Borehole-Fluid Effect Correction (BFEC) Resulting in Improved Apparent-Velocity Values

We investigate the wave propagation between the transmitter and receiver boreholes by including the refractions that occur on the boundaries between media having different wave velocities under the assumption of the far-field regime and low electrical conductivity. We use Snell's law that describes the refraction at the borehole interface as the ratio of the sinus of the incident angle ϕ_1 divided by the sinus of the transmitted angle ϕ_2, which equals the ratio of the two velocities or the inverse ratio of the squares of the relative permittivity ε_r in the borehole-fluid ε_1 and subsurface ε_2 [26]:

$$\frac{\sin \emptyset_1}{\sin \emptyset_2} = \frac{v_1}{v_2} = \sqrt{\frac{\varepsilon_2}{\varepsilon_1}}, \quad (1)$$

where $sin\ \phi_1$ and $sin\ \phi_2$ are the incident and transmitted angles with electromagnetic wave velocities v_1 and v_2 in the borehole and subsurface, respectively. Similarly, we can write for the interface between the subsurface (ε_2) and the receiver borehole with borehole fluid ε_3 and transmitted angle of ϕ_3 as follows:

$$\sin \emptyset_3 = \sin \emptyset_2 \times \sqrt{\frac{\varepsilon_2}{\varepsilon_3}}. \quad (2)$$

Another fundamental law that we consider in our correction method is total internal reflection, which could only occur when electromagnetic waves travel from a medium with lower velocity to a medium with higher velocity. Equation 3 shows the critical angle for electromagnetic waves travel from a first medium with ε_1 to a second medium with ε_2 where $\varepsilon_2 > \varepsilon_1$,

$$\emptyset_{cr.} = \text{Arcsin}\left(\sqrt{\frac{\varepsilon_2}{\varepsilon_1}}\right). \quad (3)$$

No refraction occurs when the transmitter and receiver are at equal depth and rays are traveling horizontally. In the following, we will introduce three possible ray paths that can be used to describe or approximate this phenomenon as presented in Figure 1a.

When the medium properties in the boreholes and the medium between the boreholes are equal or we ignore any refraction that is occurring, we can assume a straight line between the transmitter and receiver. We refer to this ray path model in the following as "no refraction" (N), see also Figure 1b. For the borehole fluid (e.g., water) and subsurface relative permittivities are $\varepsilon_1 = 80$ and $4 < \varepsilon_2 < 30$, respectively, the equation 3 restricts the ϕ_1^S (or ϕ_1^S) and we obtain a small ratio in equation 1. When we approximate this ratio as being zero, the incident angle equals zero ($\phi_1^S = 0$). We refer to this ray path model as "simple refraction" (S). The approximated refraction point (RP^S) is located at the same depth of the transmitter or receiver at the interface between the borehole and subsurface. For the two ray path models discussed before, the traveltime can be easily calculated as a function of the vertical distance between the transmitter and receiver (h) and the horizontal distance between transmitter and receiver that includes the distance between the two boreholes (d_{subs}) and radius of the boreholes (r_b), which we assume to be equal. We introduce a simple borehole-fluid effect correction (simple BFEC), where the traveltimes in the fluid-filled boreholes are

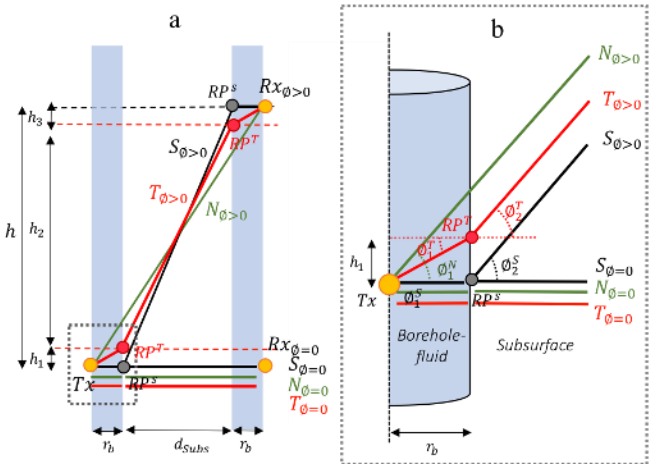

Fig. 1. a) Ray paths with no refraction (N), true refraction (T), and simple refraction (S) for zero-degree ($\phi = 0$) and arbitrary ($|\phi| > 0$) ray angle b) Close up view of the ray-paths at the interface between the borehole-fluid and the subsurface where the refraction point for simple refraction and true refraction are indicated by (RP^S) and (RP^T), respectively.

subtracted from the total traveltime and the transmitter and receiver antennas are relocated at the location of the approximated refraction points (RP^S) to calculate the apparent velocity. For the "True refraction" (T) ray path model, we consider all refractions at all interfaces, and the traveltime cannot be analytically determined since it depends on the angle (ϕ_1) that is unknown and needs to be estimated first. Therefore, we project all travelpaths to the vertical axis as follows:

$$h = h_1 + h_2 + h_3 \quad (4)$$
$$h = r_b \times \tan \emptyset_1 + d_{subs} \times \tan \emptyset_2 + r_b \times \tan \emptyset_3, \quad (5)$$

where h, h_1, h_2 and h_3 are vertical projections of the distance traveled in the first borehole, subsurface, and second borehole, respectively (see Figure 1). We substitute ε_1 and ε_3 with ε_{water} and ε_2 with ε_{subs} in equations 1 and 2, followed by their substitution into equation 5, to obtain the following equation:

$$h = 2 \times \left(\frac{r_b \times \sin \emptyset_1}{\sqrt{1-(\sin \emptyset_1)^2}}\right) + \left(\frac{d_{subs} \times \sin \emptyset_1 \times \sqrt{\varepsilon_{water}}}{\sqrt{\varepsilon_{subs} - \varepsilon_{water} \times (\sin \emptyset_1)^2}}\right), \quad (6)$$

from which, combine by the restriction determined by the equation 3; we can numerically solve ϕ_1 by assuming a known ε_{subs}. When ϕ_1 is known, we can calculate the travel distances inside the boreholes and the corresponding traveltimes. When we subtract these from the total travel distances and traveltimes, respectively, and relocate the transmitter and receiver positions to the refraction-point locations at the borehole/subsurface interface, corrected apparent velocities of the subsurface can be obtained that are not influenced by the presence of the borehole fluid (see Figure 1b).

While the horizontal distance of the refraction-point from the transmitter (or receiver) is constant and equal to the radius of the borehole r_b, the vertical difference h_1 (or h_3) is depending on the refraction that is depending on the borehole fluid, subsurface velocity and the radius of the borehole r_b. Therefore, for each single transmitter-receiver combination, there will be a different refraction point (RP^T). In principle, all transmitter and receiver locations can be updated towards the true refraction points (RP^T) however, this will result in transmitter and receiver positions that change depending on which direction the wave is emitted or received. Depending on which transmitter-receiver combination is used, the h_1 (or h_3) corrections are varying for different depths between 0.0 m to 3 m for the setup discussed here. To have one fixed position for each transmitter and receiver, we averaged the h_1's (or h_3's) corrections for each transmitter (and receiver) separately and fixed the depth of the refraction points (RP^T) for each transmitter (and receiver). Note that the maximum difference between the averaged h_1 (or h_3) and the true refraction point (RP^T) is limited to 0.015 m for this study. This averaging procedure enables us to use conventional ray-based inversion methods after the correction without unnecessarily complicated bookkeeping of the transmitter and receiver positions caused by these small variations in depths. We term the above mention method as true BFEC.

It is important to note that, for the borehole fluid (e.g., air) with relative permittivity lower than subsurface, the equation 3 restricts the ϕ_2, which means the significant vertical raise in the subsurface should happen inside the boreholes h_1 (or h_3). Therefore, the refraction points (RP^T), move drastically alongside the borehole interface by increasing the ϕ_1; thereby, our correction method could not be extended to the air-filled boreholes without modification.

III. Detailed 3D FDTD Modeling

To investigate the cause of the increasing apparent velocity with increasing ray path angle, we use a detailed model that is able to include all the possible explanations given in the literature, such as the presence of the borehole, borehole-fluid and the presence of FLA transmitter and receiver. Here, we use gprMax3D [27], which is a wave-propagation simulator that is using the FDTD method, and is particularly optimized for the modeling of GPR waves.

GprMax3D is automatically insure that the Courrant, Freidrichs and Lewy (CFL) stability condition is always meet by restricting the temporal sampling based on the spatial sampling, while using perfectly matched layers (PML) that absorb any impinging wave on the boundary of the computational domain. GprMax3D has been often used for GPR wave modeling, returns a stable solution and was already used to calculate the wave propagation for detailed antenna models [28], [29], which makes it especially suited for our purpose. All computations were carried out on JURECA cluster [30], which is part of the Jülich Supercomputing Centre (JSC). It is equipped with 1872 computing nodes with two Intel Xeon (E5-2680) with 2x12 cores, 2.5 GHz with simultaneous multithreading and DDR4 (2133 MHz) memory with various capacity from 128 to 512 GiB memory.

A. Antenna Model

We build a 3D model of resistive-loaded finite-length antenna (RLFA) from Sensors and Software crosshole 200 MHz PulseEKKO based on the information that the manufacturer supplied us. The antennas have a 0.02 m radius and a total length of 1.21 m similar to design by [31]. We used a ricker waveform excitation with specified center frequency of 92 MHz. At each side of the 0.01 m vacuum feeding point that is present at 0.26 m from the bottom of the antenna, resistively loaded arms with a length of 0.24 m are present. A Perfect Electrical Conductor (PEC) material is used as transmission wire that contained 10 resistor segments with constant electrical conductivity (σ) of 0.1 mS/m for each of the two antenna arms. As indicated by the manufacturer, this PEC is surrounded by an insulation having $\varepsilon_r = 4$ and $\sigma = 10^{-7}$ mS/m as reported by [32].

The performance and coupling of the RLFLA as a transmitter and a receiver were successfully tested by the fact that increasing ε_r values of the 3D medium surrounding the antennae resulted in a decreasing effective center frequency due to the antennas being electrically longer. Extending the model by including boreholes that are air and water-filled returned changes in arrival time, received amplitude, and center frequency shift, similar as reported by [33]. These results indicate that our detailed 3D FDTD model including RLFLA as transmitter and receiver and borehole fluid that are placed in an air- or water-filled borehole is able to return reliable synthetic data that include all the physics that is important to investigate the origin of the increasing apparent velocity with increasing ray-angle. Moreover, we studied the effect of the discretization size on the performance of the models for 0.07 – 0.09 m mesh size, and it showed the normalized waveform are similar regardless of the mesh size (not shown). Thus, the geometry of the crosshole setup, eliminate the possible staircase effect of the coarse meshing

because boreholes and the antennas are in the same plane and located in parallel to each other.

B. Homogeneous Subsurface Model

We construct a 3D subsurface model similar to the dimensions as investigated by [14] returning increasing apparent velocities as it is described. These data were measured at the Boise Hydrogeophysical Research Site near Boise, Idaho in the United States where a shallow unconfined aquifer consists of an approximately 18-m-thick layer of coarse, unconsolidated, braided-stream deposits (gravels and cobbles with sand lenses), which is underlain by clay and basalt. Therefore, our 3D gprMax3D model has dimensions of 5.5 m × 2.0 m × 22.0 m and a uniform 0.01 m discretization. It consists of 1 m layer of air with dielectric relative permittivity ε_r = 1 on top, 3 m unsaturated gravel with ε_r = 5, a 15 m layer of saturated gravel with ε_r = 12.15, and at the bottom 3 m layer of clay bedrock

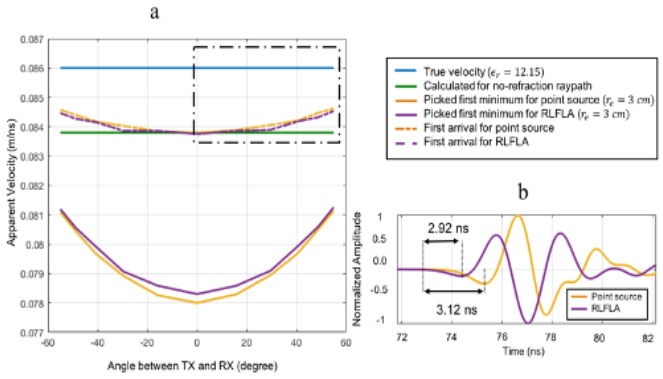

Fig. 2. a) Average apparent-velocities obtained from picked first minimums for point source (orange) and RLFLA (purple) antennas. The first arrival traveltime for point source and the first arrival traveltime with compensation for antenna thickness for RLFLA are indicated by the orange and purple dashed lines, respectively. Calculated apparent-velocities for ray paths without refraction are shown by the green line, whereas the true velocity of the medium is indicated by the blue line. b) Picked first minimum for point source and RLFLA and compensation for antenna-thickness that causes an earlier arrival for RLFLA due to the lower ε_r of the antenna insulation than borehole-fluid.

with ε_r = 18. Two 18-m-deep boreholes are present with 3.5 m distance and inner radius of 0.05 m that create.

We build a model by considering the inner radius of the borehole filled with water in the saturated area ε_r = 80 and the air-filled area of ε_r = 1. Since the RLFLA has radius of 0.02 m, therefore the effective radius of the model including the FLRLA is 0.03 m. Because the point source antenna has no dimension, we used the borehole with 0.03 m inner radius for the point source model to be consistent and comparable with the results of the RLFLA.

We put a transmitter located at a depth of 11 m and placed 12 receivers from 6 m to 17 m depth in the homogenous saturated gravel layer. This setup geometry provides us an angular coverage of -60 to +60 degree. We carried out separate simulations for each transmitter – receiver position pair and for a point source and RLFA.

We used a manual picking method to pick the first local minimum. The two lower curves in Figure 2a show the apparent velocities for the picked minima (that is later used to calculate the corrected first break) from the modeled point source (orange line) and RLFLA (purple line) data. An increasing apparent velocity for increasing ray path angle is observed similar to [14]. As shown in Figure 2b, the first minima of the RLFLA arrives slightly earlier than for the point source. This is due to the different effective wavelets that are emitted/received by the point transmitter/receiver and the RLFLAs, and the antenna insulation thickness which has lower relative permittivity in compare to the subsurface that causes a constant drift between the two lower curves of Figure 2a. When we compensate for the first local minima arrival within the waveform and the constant shift caused by the antenna-insulation thickness; we obtain almost overlying apparent-velocity curves (see Figure 2a).

These results show that the increasing apparent velocity with increasing ray path angle is not caused be the RLFLA since both point source/receiver and RLFLAs show very similar results. Comparing the obtained results with the true velocity of the medium, we see that the results are still significantly off. The corrected point source/receiver and RLFLA's results for zero-angle ray paths and "no refraction" ray-based model (N) are equal since no refraction occurs for horizontally traveling waves. Note that the apparent-velocity values are lower than the true velocity due to the presence of the water in the boreholes. We studied the possible effect of the borehole casing by adding a 0.01 m plastic casing of ε_r = 4, resulting in an earlier wave arrival due to the lower permittivity of the casing material compared to the subsurface, but still the same trend of increasing apparent velocity with increasing ray path angle is observed (not shown). When investigating the effect of the borehole radius on the apparent-velocity by increasing the radius from 0.05 m to 0.09 m, an increasing apparent-velocity range from 3.6% to 7% is observed. These results are consistent with the observations as described by [33]. It is important to note that the smaller variation range of the simulation results in

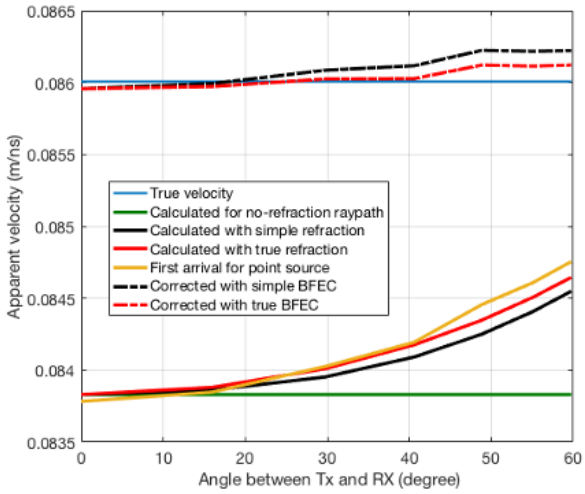

Fig. 3. Average apparent-velocities of first arrival for point source (orange), assuming no refraction (green) and true velocity (blue) as shown in Figure 2a in the dashed rectangle. Calculated simple refraction apparent-velocities (black line) approach the first arrival values, whereas the true refraction apparent-velocities (red line) comes very close to first arrival values of the point source. Applying the simple BFEC and true BFEC returns apparent-velocities indicated by the dashed black and red lines, respectively, that approach the true velocity.

comparison to inversion results for measured data such as [14] because we used a homogenous subsurface, while the presented data were measured in a natural site including a natural heterogeneity.

Due to symmetry, we show the Figure 2a zoomed in a version in Figure 3a for positive transmitter-receiver ray paths angles. Moreover, we limit our analysis to the point-source arrival due to the results' similarity with the RLFLA. The simple BFEC angle-dependent apparent-velocities (S, black line) approach the first arrival, whereas the true BFEC apparent velocities (T, red line) are almost overlying the first arrival for point source. These results show that the increase in apparent velocity for increasing ray-angle is caused by the wave refraction, when propagating from the water-filled borehole into the subsurface for the transmitter antenna and vice versa for the receiver antenna borehole. We apply the BFEC for simplified and true refraction ray paths as discussed in the previous section to obtain the corrected apparent velocity for each transmitter-receiver pairs. The simple BFEC results approach the true apparent-velocity values whereas the true BFEC results are almost overlying the true velocity of the medium as indicated by the blue line in Figure 4. The maximum errors in apparent-velocity reduced from 3.6% to 0.25% for the simple BFEC approach for the highest studied ray path angle of 60°, whereas the true BFEC has only 0.14% error. These results show that the presence of the water-filled boreholes results in a large decrease in apparent-velocities for zero-angle rays due to a relatively large travel path through the water-filled borehole, whereas the apparent velocity decrease for high-angle rays is less due to a relatively short travel path through the water-filled borehole. Note that the increased apparent velocities for increasing ray-angle are closer to the true apparent velocity than the zero-ray apparent velocity. By using the BFEC approach, high-angle ray paths can now reliably be included in ray-based tomography inversion approaches without any artifacts. For seismics, the refraction at the borehole interface is much less and strong ray-angle dependent apparent-velocity changes are not expected, which was also confirmed by [17].

When solving equation 6, we assume to know ε_{subs}. Here, we carry out a sensitivity analysis to study the importance of the assumed ε_{subs} on the performance of the BFEC. We apply the BFEC for a range between -50% to +50% of the true value of ε_{subs}. Figure 5 shows the relative error in estimated apparent velocities for the simplified and true BFEC method with different ε_{subs} values. The model errors for the true refraction method is fluctuating between 0.05% to 0.17% depending on ε_{subs}, while the maximum model error is limited to the model error of the simple BFEC which is ~0.25% for the highest studied angle.

C. Heterogeneous Subsurface Model of River Thur Test Site

To investigate the influence of heterogeneity, we construct a 3D subsurface model of the well-known aquifer system of the test site near the river Thur in Switzerland [34], [35]. This glaciofluvial deposit contains a 7 m gravel layer embedded between 3 m alluvial loam at the top and a low permeable clay aquitard below 10 m depth. The water table is at 4 m depth except during river-flood events. Previous studies [36], [37] indicated the presence of a high-velocity layer overlying a low-velocity layer between 4 m - 6 m depth, a high velocity layer with low conductivity between 6 m - 8 m, and intermediate values for both parameters below 8 m depth (Figure 5a). The boreholes are 5 m apart with 10 m depth and have a diameter of 0.12 m. Data were acquired for 11 transmitter positions with 0.5 m interval and 57 receiver positions with 0.1 m spacing in each borehole with a semi-reciprocal approach, where all transmitters and receivers were located in the saturated zone.

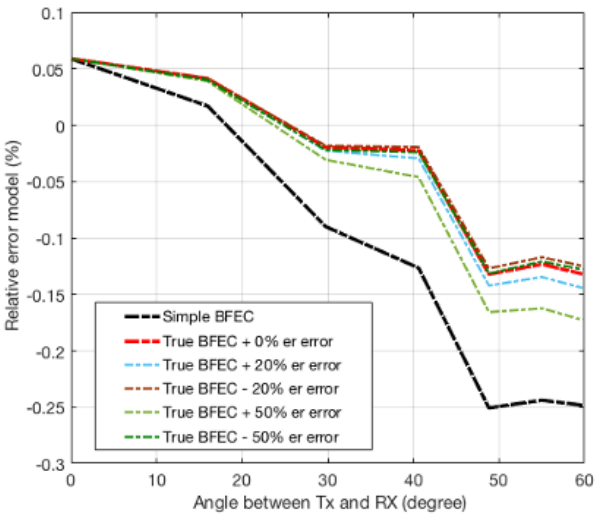

Fig. 4. Relative model errors in estimated apparent velocity as a function of the ray path angle for the simple BFEC and true BFEC with -50% to 50% error in the ε_{subs}.

Our subsurface gprMax3D model has dimensions of 7.02 m × 0.9 m × 11.7 m and a uniform 0.01 m discretization including two 0.06 m radius water-filled boreholes with effective radius of 0.04 m. We use the ε_r and σ values as obtained by [36] as a model to generate 2508 traces using the same transmitter and receiver spacing as the experimental studies (see Figure 5a). In addition, we build an identical model, where no borehole is present, and, one where we embedded the RLFLA a in the subsurface with no borehole. The last model we use as benchmark for the performance of the BFEC corrections.

We use a manual picking method to locate the first break. Then, we apply the simple and true BFEC on the data where traveltimes in the boreholes for each transmitter and receiver pair are calculated and deducted from the corresponding picked traveltimes. In addition, we relocate the position of each transmitter and receiver at the borehole/subsurface interface depending on the simple or true BFEC (see Figure 1b). Finally, we invert the picked and corrected picked data using the curved-ray-based traveltime inversion [38], [39] where the domain between the boreholes is discretized to 72×80 cells. We obtain the lowest root-mean-square (RMS) values for a damping and smoothing factor of 1 and a homogenous starting model with constant relative permittivity of 18.

Relative-permittivity tomograms obtained from the picked data for no borehole presence, water filled boreholes without

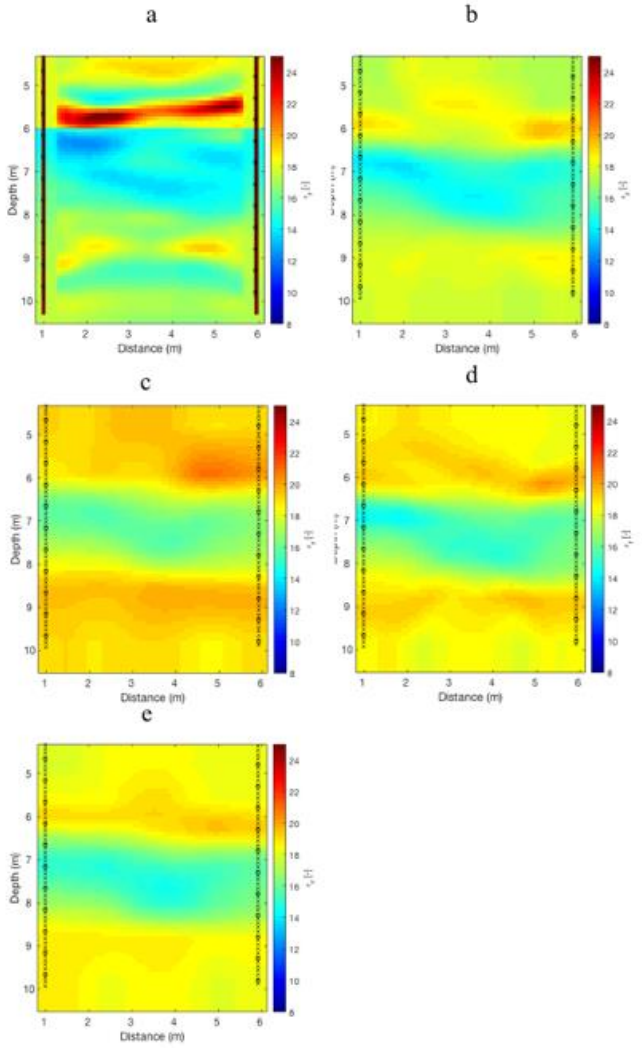

Fig. 5. Relative permittivity tomogram of a) reference model based on [36] where the water-filled boreholes are indicated by two yellow lines, b) traveltime inversion tomogram for no borehole, c) traveltime inversion tomogram for water-filled borehole without BFEC and c) traveltime inversion tomogram for water-filled borehole with simple BFEC, e) traveltime inversion tomogram for water-filled borehole with true BFEC. Transmitter and receiver positions are indicated by circles and crosses, respectively.

BFEC, water filled boreholes with simple and true BFEC are presented in Figure 5 where we interpolate the results to the cell-size of the forward model for comparison reasons. As expected, relative-permittivity tomogram of the no borehole data is closest to the reference subsurface model. Almost all relative-permittivity values for the data without BFEC have a larger value than the true model, whereas the data with the simple and true BFEC approaches the reference model better. This is consistent with the apparent velocity being too low when using uncorrected data.

Figures 6a – 6d show the relative model error distributions of the estimated relative permittivity for no borehole, water-filled boreholes without BFEC, water-filled boreholes with simple and true BFEC, respectively. It showed that a better reconstruction when using the simple or true BFEC data, in compare to the water filled data without BFEC. Figures 6e and 6f show the mean horizontal and vertical model error, respectively, in estimated relative permittivity. Both mean vertical and horizontal relative error models are lower for the picked data with simple and true BFEC. The mean relative model error in the entire domain is 4% for no borehole, 13% for the water-filled borehole without BFEC, 9% for simple BFEC and 8% for true BFEC. In order to study the effectivity

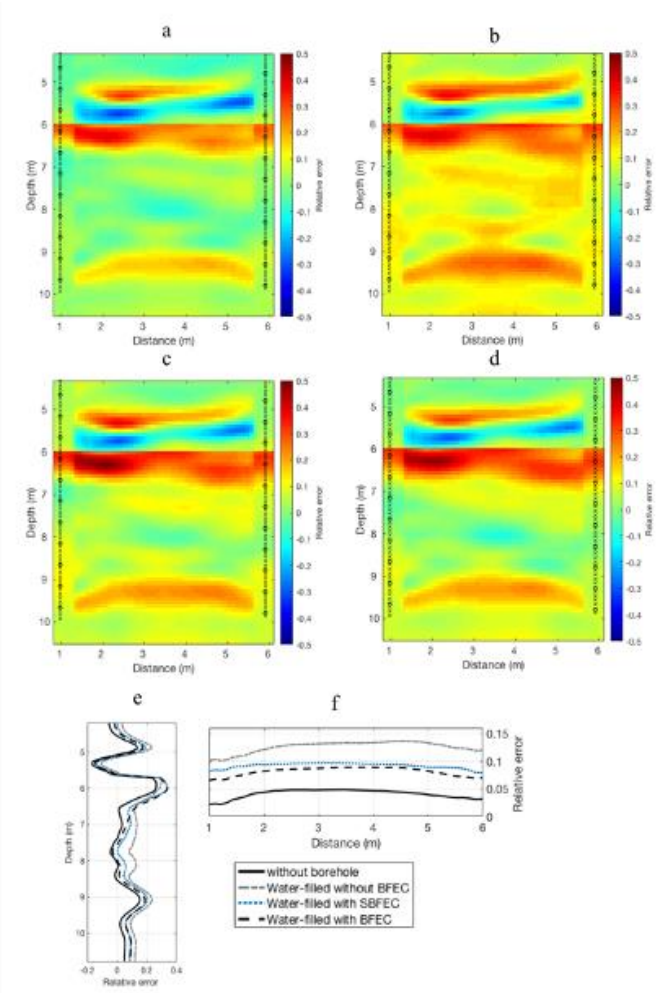

Fig. 6. Relative model error in estimated permittivity for a) traveltime inversion for no borehole b) traveltime inversion for water-filled borehole without BFEC c) traveltime inversion for water-filed borehole with simple BFEC, d) traveltime inversion for water-filed borehole with BFEC,, e) mean relative model error in estimated relative permittivity in vertical cross-section between two boreholes and f) mean relative model error in estimated relative permittivity in horizontal cross-section between two boreholes. Tomogram for water-filled borehole with true BFEC. Transmitter and receiver positions are indicated by circles and crosses, respectively.

of the BFEC, we calculate the model difference percentage of the water-filled boreholes without BFEC, the water-filled boreholes with the simple and true BFEC in compare to the no borehole scenario, since the ultimate aim of the BFEC is to compensate for the presence of the borehole, in the way that results are close to no borehole data. As it showed in the Figure 7, relative difference to the no borehole result is decreased by using the simple and true BFEC. The mean relative model differences in the entire domain are 5.1%, 3% and 2.4% for water-filled boreholes without BFEC, water filled boreholes with simple BFEC and water-filled boreholes with true BFEC, respectively which shows that applying the BFEC compensate for the effect of the borehole presence in the data. Note that to obtain higher resolution images a full-

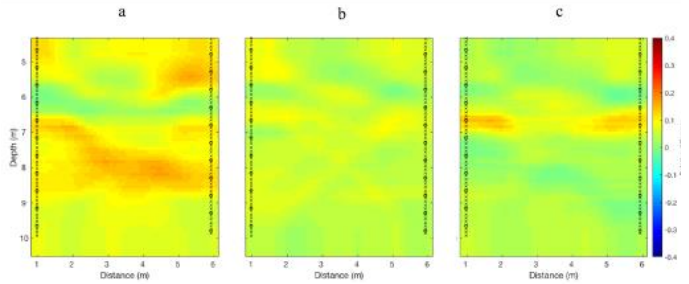

Fig. 7. Relative difference in estimated permittivity of no borehole case in compare to a) traveltime inversion without BFEC b) traveltime inversion with simple BFEC and c) traveltime inversion with true BFEC. Transmitter and receiver positions are indicated by circles and crosses, respectively.

waveform inversion can be carried out [37], where it is also important to have a good starting model as has been obtained here.

IV. Conclusions

Detailed 3D electromagnetic modeling of crosshole GPR waves including borehole-fluid and resistive loaded finite-length antenna (RLFLA) has been used to investigate the refraction of the electromagnetic waves at the borehole interface between water and subsurface as significant contributor to increase of apparent velocities for increasing ray path angles often observed in GPR crosshole data. The performed modeling points out that this phenomenon is majorly influenced by refraction at the borehole interface between water and subsurface. Because of the substantial change in wave velocity in the borehole fluid compared to the wave velocity in the saturated subsurface medium present between the boreholes, the apparent velocity is increasing for increasing ray-angle, whereas the effect is amplified for larger borehole radius and causes larger apparent-velocity differences. Since the velocity changes at the borehole interface are much more substantial for GPR compared to seismic tomograms, the phenomenon is mainly present for GPR and has not been observed for seismic crosshole measurements.

Synthetic studies show that due to the water-filled borehole and the pertaining refraction on the interface between the borehole and the subsurface conventionally obtained velocities are always lower than the real values. We introduce a simple borehole-fluid effect correction (BFEC) and a true BFEC method that use an approximated and true refraction at the borehole interfaces between the water and subsurface, respectively. In this way, reliable apparent velocity values are obtained. For a homogeneous model, maximum errors in the apparent velocity of the medium between water-filled boreholes with a radius of 0.05 m reduced from 3.6% to 0.25% and 0.14% for the simple BFEC and true BFEC approach, respectively. We verified the performance of the simple BFEC and true BFEC for synthetic heterogeneous crosshole data based on realistic full-waveform inversion results from the river Thur in Switzerland. By applying identical damping and smoothing parameters in curved-ray-based traveltime inversion without BFEC, with the simple BFEC and true BFEC, the subsurface structures were reconstructed with more details for the simple BFEC and true BFEC data and the average relative error model reduced from 13% to 9% and 8% with simple BFEC and true BFEC, respectively, despite using an approximation to relocate the transmitter and receiver positions at the refraction points.

We show that instead of excluding high-angle ray paths from ray-based inversions, commonly used to prevent artifacts, our novel BFEC method enables the use of an increased ray-angle range which results in more-accurate and higher-resolution tomographic inversion results.

V. Acknowledgement

The authors gratefully acknowledge the computing time granted by the John von Neumann Institute for Computing (NIC) and provided on the supercomputer JURECA at Jülich Supercomputing Centre (JSC). We thank Peter Annan for helping us in the early stage of this study.

References

[1] J. Tronicke and Klaus Holliger, “Multivariate analysis of cross-hole georadar velocity and attenuation tomograms for aquifer zonation,” *Water Resour. Res.*, vol. 40, pp. 1–14, 2004.

[2] C. Dorn, N. Linde, T. Le Borgne, O. Bour, and L. Baron, “Single-hole GPR reflection imaging of solute transport in a granitic aquifer,” *Geophys. Res. Lett.*, vol. 38, no. 8, pp. 1–5, 2011.

[3] A. Klotzsche, F. Jonard, M. C. Looms, J. van der Kruk, and J. A. Huisman, “Measuring Soil Water Content with Ground Penetrating Radar: A Decade of Progress,” *Vadose Zo. J.*, vol. 17, 2018.

[4] G. A. Meles, J. Van Der Kruk, S. a. Greenhalgh, J. R. Ernst, H. Maurer, and A. G. Green, “A new vector waveform inversion algorithm for simultaneous updating of conductivity and permittivity parameters from combination crosshole/borehole-to-surface GPR data,” *IEEE Trans. Geosci. Remote Sens.*, vol. 48, no. 9, pp. 3391–3407, 2010.

[5] W. Menke, “The resolving power of cross-borehole tomography,” *Geophys. Res. Lett.*, vol. 11, pp. 105–108, 1984.

[6] N. . Bregman, R. C. Bailey, and C. H. Chapman, “Ghosts in tomography: The effects of poor angular coverage in {2-D} seismic traveltime inversion,” *J. Can. Soc. Expl. Geophys.*, vol. 25, no. 1, pp. 7–27, 1989.

[7] J. W. Rector and J. K. Washbourne, “Characterization of resolution and uniqueness in crosswell direct-arrival traveltime tomography using the Fourier projection slice theorem,” *GEOPHYSICS*, vol. 59, no. 11, pp. 1642–1649, 1994.

[8] B. A. Hardage, *Crosswell seismology & reverse VSP*. Geophysical Press, 1992.

[9] P. R. Williamson and M. H. Worthington, “Resolution limits in ray tomography due to wave behavior: Numerical experiments,” *Geophysics*, vol. 58, no. 5, p. 727, 1993.

[10] A. Becht, J. Tronicke, E. Appel, and P. Dietrich, “Inversion strategy in crosshole radar tomography using information of data subsets,” *Geophysics*, vol. 69, no. 1, p. 222, 2004.

[11] S. Ebihara and Y. Hashimoto, “MoM analysis of dipole antennas in crosshole borehole radar and field experiments,” *IEEE Trans. Geosci. Remote Sens.*, vol. 45, no. 8, pp. 2435–2450, 2007.

[12] R. Streich and J. Van Der Kruk, “Accurate imaging of Multicomponent GPR data based on exact radiation patterns,” *IEEE Trans. Geosci. Remote Sens.*, vol. 45, no. 1, pp. 93–103, 2007.

[13] J. E. Peterson, “Pre-inversion corrections and analysis of radar tomographic data,” *J. Environ. Eng. Geophys.*, vol. 6, no. 1, pp. 1–18, 2001.

[14] J. D. Irving, M. D. Knoll, and R. J. Knight, “Improving crosshole radar velocity tomograms: A new approach to incorporating high-angle traveltime data,” *Geophysics*, vol. 72, no. 4, pp. J31–J41, 2007.

[15] D. Alumbaugh, P. Y. Chang, L. Paprocki, J. R. Brainard, R. J. Glass, and C. A. Rautman, “Estimating moisture contents in the vadose zone using cross-borehole ground penetrating radar: A study of accuracy and repeatability,” *Water Resour. Res.*, vol. 38, no. 12,

p. 1309, 2002.

[16] J. D. Irving and R. J. Knight, "Effect of antennas on velocity estimates obtained from crosshole GPR data," *Geophysics*, vol. 70, no. 5, pp. K39–K42, 2005.

[17] G. J. Moret, M. D. Knoll, W. Barrash, and W. P. Clement, "Investigating the stratigraphy of an alluvial aquifer using crosswell seismic traveltime tomography," *Geophysics*, vol. 71, no. 3, pp. B63–B73, 2006.

[18] D. Alumbaugh, P. Y. Chang, D. LaBrecque, and M. Stuben, "Investigating Vadose-zone flow and transport processes using cross borehole GPR and electrical resistivity," 2003.

[19] N. Linde, S. Finsterle, and S. Hubbard, "Inversion of tracer test data using tomographic constraints," *Water Resour. Res.*, vol. 42, no. 4, pp. 1–15, 2006.

[20] M. C. Looms, T. M. Hansen, K. S. Cordua, L. Nielsen, K. H. Jensen, and A. Binley, "Geostatistical inference using crosshole ground-penetrating radar," *Geophysics*, vol. 75, no. 6, pp. J29–J41, 2010.

[21] G. Pirot, N. Linde, G. Mariethoz, and J. H. Bradford, "Probabilistic inversion with graph cuts: Application to the Boise Hydrogeophysical Research Site," *Water Resour. Res.*, vol. 53, no. 2, pp. 1231–1250, 2017.

[22] M. A. McGlashan, G. P. Tsoflias, P. C. Schillig, J. F. Devlin, and J. A. Roberts, "Field GPR monitoring of biostimulation in saturated porous media," *J. Appl. Geophys.*, vol. 78, pp. 102–112, 2012.

[23] R. N. Lassen, T. O. Sonnenborg, K. H. Jensen, and M. C. Looms, "Monitoring CO2 gas-phase migration in a shallow sand aquifer using cross-borehole ground penetrating radar," *Int. J. Greenh. Gas Control*, vol. 37, pp. 287–298, 2015.

[24] K. S. Cordua, T. M. Hansen, K. Mosegaard, and T. U. Denmark, "Monte Carlo full waveform inversion of tomographic crosshole data using complex geostatistical a priori information Monte Carlo full waveform inversion," pp. 4291–4296, 2010.

[25] J. Keskinen *et al.*, "Full-waveform inversion of Crosshole GPR data: Implications for porosity estimation in chalk," *J. Appl. Geophys.*, vol. 140, pp. 102–116, 2017.

[26] A. Glassner, *An Introduction to Ray Tracing*. Morgan Kaufmann, 1989.

[27] C. Warren, A. Giannopoulos, and I. Giannakis, "gprMax: Open source software to simulate electromagnetic wave propagation for Ground Penetrating Radar," *Comput. Phys. Commun.*, vol. 209, pp. 163–170, 2016.

[28] C. Warren and A. Giannopoulos, "Creating finite-difference time-domain models of commercial ground-penetrating radar antennas using Taguchi's optimization method," *Geophysics*, vol. 76, no. 2, 2011.

[29] I. Giannakis, A. Giannopoulos, and C. Warren, "Realistic FDTD GPR antenna models optimised using a novel linear / non-linear Full Waveform Inversion," *IEEE Trans. Geosci. Remote Sens.*, vol. PP, pp. 1–11, 2018.

[30] D. Krause and P. Thörnig, "JURECA: General-purpose supercomputer at Jülich Supercomputing Centre," *J. large-scale Res. Facil. JLSRF*, vol. 2, p. A62, 2016.

[31] S. Ebihara and Y. Inoue, "Analysis of eccentered dipole antenna for borehole radar," *IEEE Trans. Geosci. Remote Sens.*, vol. 47, no. 4, pp. 1073–1088, 2009.

[32] B. Lampe and K. Holliger, "Resistively loaded antennas for ground-penetrating radar: A modeling approach," *Geophysics*, vol. 70, no. 3, pp. K23–K32, 2005.

[33] J. Tronicke and K. Holliger, "Short Note Effects of gas- and water-filled boreholes on the amplitudes of crosshole georadar data as inferred from experimental evidence," *Geophysics*, vol. 69, no. 5, pp. 1255–1260, 2004.

[34] J. Doetsch, N. Linde, I. Coscia, S. A. Greenhalgh, and A. G. Green, "Zonation for 3D aquifer characterization based on joint inversions of multimethod crosshole geophysical data," *Geophysics*, vol. 75, no. 6, pp. 53–64, 2010.

[35] I. Coscia *et al.*, "3D crosshole ERT for aquifer characterization and monitoring of infiltrating river water," *Geophysics*, vol. 76, no. 2, pp. G49–G59, 2011.

[36] A. Klotzsche, J. Van Der Kruk, G. Meles, H. Vereecken, and J. van der Kruk, "Crosshole GPR full-waveform inversion of waveguides acting as preferential flow paths within aquifer systems," *Geophysics*, vol. 77, no. 4, p. H57, 2012.

[37] A. Klotzsche, J. Jan van der, Kruk, L. Niklas, J. Doetsch, and H. Vereecken, "3-D characterization of high-permeability zones in a gravel aquifer using 2-D crosshole GPR full-waveform inversion and waveguide detection," *Geophys. J. Int.*, vol. Vol.195, no. No.2, pp. 932–944, Aug. 2013.

[38] E. Lanz, H. Maurer, and A. G. Green, "Refraction tomography over a buried waste disposal site," *Geophysics*, vol. 63, no. 4, pp. 1414–1433, 1998.

[39] J. Tronicke, D. R. Tweeton, P. Dietrich, and E. Appel, "Improved crosshole radar tomography by using direct and reflected arrival times," *J. Appl. Geophys.*, vol. 47, no. 2, pp. 97–105, 2001.